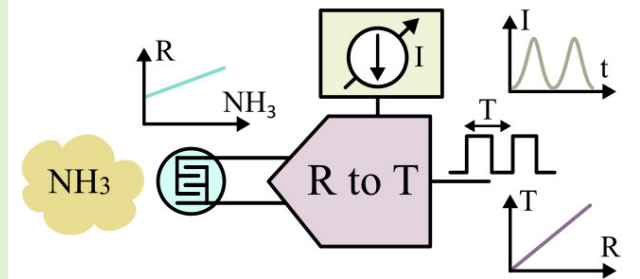


Design of Ultralow-Power Sensor Readout Circuits Through Adaptive Biasing for Gas Monitoring With Chemiresistive Sensors

Rafael Puyol^{ID}, Member, IEEE, Thomas Walewyns^{ID}, Laurent A. Francis^{ID}, Member, IEEE, and Denis Flandre^{ID}, Senior Member, IEEE

Abstract—This article presents two adaptive biasing techniques for comparators to achieve ultralow-power and high dynamic range in readout circuits for resistive gas sensors. The first technique is based on an on-demand biasing that generates a bias current up to $3 \mu\text{A}$ when the differential input voltage is close to zero, while minimizing the bias current when a comparison is not imminent. The second technique takes advantage of the correlation between sensor current and delay requirements to bias the comparator with the appropriate current for each situation. These techniques were applied to two readout circuits, demonstrating a reduction of the energy per measurement to less than a fifth for the largest input resistance in comparison to fixed biasing without affecting SNR. The input range is above five decades in both cases, from $2.4 \text{ k}\Omega$ up to $1 \text{ G}\Omega$ and from $1 \text{ k}\Omega$ up to $270 \text{ M}\Omega$. The signal to noise ratio ranges from 55 dB up to 70 dB which provides enough margin to interface a wide range of gas sensors. Lastly, one of the designs was successfully employed to measure varying concentrations of ammonia with a polypyrrole (PPy) gas sensor.



Index Terms—Gas detectors, low-power electronics, sensor readout systems, sensor systems and applications.

I. INTRODUCTION

AS detection techniques date back to the late 19th century when animals like canaries or mice were used for the detection of carbon monoxide in coal mines [1]. By the turn of the 20th century, the need for detection and recognition of gases grew even more with the expansion of the oil and gas industry. Since then, their applications have broadened to

Manuscript received 7 September 2023; accepted 27 September 2023. Date of publication 13 October 2023; date of current version 14 November 2023. This work was supported in part by the BioWin Cluster BioCloud4.0 Project funded by Wallonia through the MICRO+ Project, co-funded by the European Regional Development Fund (ERDF) and Wallonia; and in part by the Agrosensor Consortium of Wagralim, Wallonia, Belgium. The associate editor coordinating the review of this article and approving it for publication was Prof. Yu-Te Liao. (Corresponding author: Rafael Puyol.)

Rafael Puyol was with the Institute for Information and Communication Technologies, Electronics and Applied Mathematics (ICTEAM), UCLouvain, 1348 Louvain-la-Neuve, Belgium. He is now with the Electrical Engineering Department, Universidad Católica del Uruguay, Montevideo 11600, Uruguay (e-mail: rpuyl@ucu.edu.uy).

Thomas Walewyns is with VOCsens, 1348 Louvain-la-Neuve, Belgium.

Laurent A. Francis and Denis Flandre are with the Institute for Information and Communication Technologies, Electronics and Applied Mathematics (ICTEAM), UCLouvain, 1348 Louvain-la-Neuve, Belgium (e-mail: laurent.francis@uclouvain.be).

Digital Object Identifier 10.1109/JSEN.2023.3322393

include environmental control, health monitoring, and machinery health management among others. This development was also accompanied by progress in the sensor's technology. Starting with catalytic sensors in the 1920s, joined by metal-oxide (MOx) in the 1960s [2], and recently by more sophisticated devices like compact nondispersive infrared (NDIR) sensors and chemiresistive sensors made with conductive polymers or graphene [3], [4].

No technology alone has been able to offer at the same time good sensitivity, selectivity, long lifespan while having a power consumption compatible with IoT systems. Photoionization and NDIR sensors require complex electronics to illuminate the gas with UV or IR light and then process the measured signal, while on the other hand, devices like MOx and electrochemical sensors are insufficiently selective as they rely on the chemical interaction between materials and gases. Additionally, the sensing mechanism of catalytic and MOx sensors is temperature dependent, and most sensitive at several hundred degrees, requiring power-hungry heating elements. With regards to the composition, noble metals are frequently used for the electrodes in electrochemical sensors and for the heater in MOx and catalytic sensors [5], resulting in costly devices.

Inspired by the human nose which contains nearly 400 different olfactory receptors that simultaneously contribute to produce different smells, researchers have tried to improve the performance of gas sensors by using arrays of dissimilar sensors in parallel [6], [7]. For this approach, chemiresistive sensors are good candidates as they are easy to miniaturize, suitable for many types of sensing layer materials, and capable of integrating the readout electronics in the same chip. The sensor's principle of operation is the change of conductance of nanoengineered materials, like polypyrrole (PPy), polyaniline (PANI), or functionalized graphene, when exposed to certain gases. A pair of interdigitated electrodes (IDEs) makes electrical contact and provides mechanical support. The chemistry and dimensions can be tuned to achieve very low area and power consumption; hence tens of sensors can be integrated into a single chip with an area of a few square millimeters as demonstrated by Le Maout et al. [8], Ge et al. [9], and Simonenko et al. [10]. On the other hand, such sensors present a challenge for the readout integrated circuit (ROIC) as the baseline resistance of each sensor can be greatly different, spanning several decades [3], [4] and increased by miniaturization. Due to power and area constraints, a single high-dynamic-range ROIC with a multiplexer is preferred, rather than a circuit for each sensor. For example, in [11], a ROIC for gas sensors achieved a 128 dB dynamic range. Going beyond this value will enable interfacing a wider range of sensor types.

ROICs used to estimate the sensor's resistance can be broadly classified into two categories: those that produce a time signal whose period (or frequency) is proportional to the measurand and those that produce a voltage amplitude. In the first case, significant work has been done with current or voltage-controlled oscillators (VCOs) both in open [6], [11], [12] and closed-loop architectures [13], [14].

Open-loop designs are simpler and offer the benefit of separating the biasing of the sensor from the rest of the circuit, imposing no restriction on the sensor bias point. On the other hand, closed-loop designs use the output frequency to adjust the sensor bias current and make the VCO operate at a fixed input voltage, avoiding the usual nonlinearity in the voltage-to-frequency conversion found for larger input swings. Both types require an additional circuit to digitize the period.

With respect to amplitude readout circuits, they measure the voltage directly with an analog-to-digital converter (ADC). Frequently, Wien bridges or current digital-to-analog converters (IDACs) are used to bias the sensor and extend the input range, as is the case of [15]. They offer good linearity but fail to achieve simultaneously high dynamic range and low power, largely explained by the large number of bits needed both in the ADC and IDAC [16], [17], [18].

To a lesser extent, other architectures like triggered ROICs have also been investigated. Woo and Yang [19] proposed a discharge time ROIC with the sensor embedded in an RC discharge circuit with an integrated capacitor. The power consumption is low, between 461.5 and 543.5 nW but their design is limited to a maximum sensor resistance of 100 k Ω and the sensor voltage bias is not kept constant. The latter is especially inconvenient because conductive polymers are

usually not ohmic materials [3], therefore, the resistance value changes during discharge and the estimation of the gas concentration from the discharge time is not obtained from the RC equations.

Other authors, like Park et al. [20], have not relied on a single approach. In their paper, they describe a multi-sensor system employing one relaxation-oscillator ROIC and one ADC ROIC, to achieve low power or high resolution as needed, even though the relaxation oscillator achieves a power consumption of just 2.95 μ W (low resolution mode), the system power consumption is much larger due to the current needed for the heater of the MEMS sensor, 118.8 μ A.

In the context of autonomous sensing nodes, several authors have studied the energy profile of low-power wireless technologies and their impact on the lifespan of the whole sensing system. For example, Bluetooth Low Energy 5.0 can transmit a total of 331 million 50-byte packets of useful data, in 10.5 years of continuous operation, at one packet per second ($P_{out} = 0$ dBm) from a pair of AAA primary cells ($E = 13.5$ kJ) as presented in [21], which translates into 816 nJ per useful byte of transmitted data. This low figure implies that the ROIC must be capable of accommodating very dissimilar sensors while minimizing power consumption to retain a long battery life.

Owing to the large variability of baseline resistance in sensors made with PPy, PANI, or graphene but also in legacy technologies like MOx [22], open-loop relaxation-oscillators offer at the same time a wide input range and bias flexibility to interface multiple sensors sequentially [20]. On the downside, this large variability impacts the time it takes to make one measurement, for example, in [23] a readout for sensors with resistances between 100 Ω and 10 M Ω is presented, with an oscillation period ranging from 100 ns to 10 ms, respectively (all other parameters remaining equal). Such wide range results in a very distinctive power consumption profile where these ROICs are highly efficient for short periods but become inefficient as the period increases and static power consumption becomes dominant. In this article, we analyze the efficiency degradation of open-loop relaxation-oscillator ROICs for high resistance sensors and propose two adaptive biasing techniques to improve power consumption that do not require external supervision and can retain the desirable input characteristics needed for autonomous multi-sensor monitoring systems. We have validated the adequacy of relaxation-oscillator as ROICs for chemiresistive gas sensors in a previous application-specific integrated circuit (ASIC) used for the monitoring of gases in the ppb range with conductive-polymer sensors [6]. Here, we depart from the classical architecture to study the boundaries of power consumption.

The content of this article is structured as follows; we begin with a brief explanation of the principle of operation of the readout circuit. Then, we analyze the power consumption and discuss the common figures of merit (FOM). Third, we propose two adaptive bias mechanisms for comparators. Afterward, we present the characterization of two read-out circuits using the proposed power reduction techniques and we show measurements with a real gas sensor. Finally, we draw some conclusions.

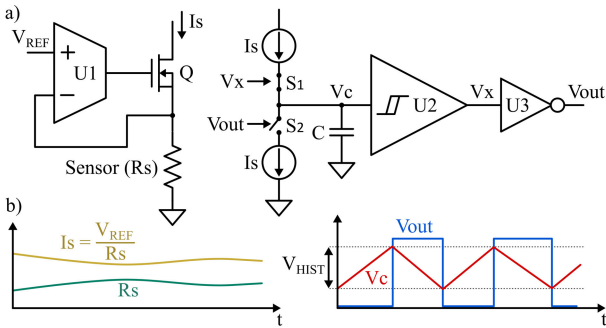


Fig. 1. (a) Simplified block diagram of a relaxation oscillator-based ROIC. (b) Signal chronograms at different nodes.

II. PRINCIPLE OF OPERATION OF RELAXATION-OSCILLATOR-BASED READOUT CIRCUITS

The principle of operation of a relaxation-oscillator-based sensor interface is depicted in Fig. 1(a). On the left side, a voltage regulator, formed by a transconductance amplifier U1 and a MOS transistor Q, sets the bias voltage of the sensor given an external reference, V_{REF}. The current flowing through Q is copied and divided by a factor δ to feed the current-controlled relaxation oscillator (CCRO).

The CCRO is made of a comparator U2 with hysteresis voltage V_{HIST}, a logic inverter U3, an integration capacitor C, and two control switches: S₁ and S₂ which transfer the current to or out of C. When the comparator output (V_x) is low, S₁ is open and S₂ closed, thus the capacitor is discharging until its voltage reaches the lower threshold of the comparator's hysteresis. At this point, the output of U2 becomes high, S₁ is closed, S₂ opened, and the capacitor begins charging. This repeats as long as the circuit is operated, Fig. 1(b). The period (1) can be calculated from the circuit parameters. Lastly, an integrated or external counter (e.g., from a microcontroller) transforms the period length into a digital value

$$T = \frac{1}{f} = \frac{2 \cdot R_s \cdot \delta \cdot C \cdot V_{HIST}}{V_{REF}}. \quad (1)$$

A. Power Consumption and Energy per Conversion

Together with standard FOMs, like static current or power consumption, one that has received significant attention is the energy per conversion (EPC) [12], [15], [24]. The EPC is the energy needed to produce an estimation of the measurand, represented as a digital number in steady state. It is similar to Walden's classic ADC FOM [25], that is sometimes used in conjunction or alternatively, but does not account for the effective number of bits (ENOBs). In open-loop readout circuits, the bandwidth and output jitter evolve throughout the input range giving a different SNR, and thus an ENOB, for each operating point. For this reason, it is sometimes preferred to study the energy profile separated from that of noise as they can be uncorrelated. Furthermore, ideally the jitter caused by readout circuits should not be larger than that caused by the sensor, so it is the sensor that will ultimately determine the SNR and thus EPC can serve as a comparison metric for the complete system. Like Walden's FOM, the EPC does not account for the

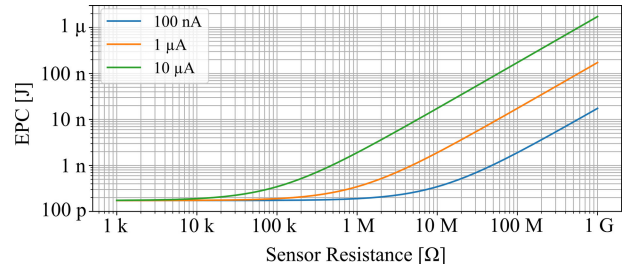


Fig. 2. Simulated EPC for three bias currents: 100 nA, 1 μA, and 10 μA. V_{REF} = 1 V, C = 8 pF, δ = 10, V_{DD} = 1.8 V, and V_{HIST} = 0.6 V.

stabilization time that is needed after power-up, nor sensor-specific variables like bias voltage, but it still captures the intrinsic efficiency of the circuit [11], [13].

The power consumption of relaxation oscillators, as depicted in Fig. 1, is distributed among its components and is highly dependent on the sensor's resistance and V_{REF}. A part of the energy is dissipated in the sensor and the rest in the readout (2)–(4). The EPC is calculated by multiplying the power associated with each functional part of the circuit by the period of operation T and adding the results (2). The power consumed due to the sensor is that of a resistor: V_{DD} · (V_{REF}/R_s), whereas that of the readout interface is the product of V_{DD} and ΣI, where ΣI denotes the sum of the bias currents of each circuit block: U1, U2, and U3. As the period is proportional to the sensor resistance (1), the energy dissipated in the sensor is constant for all R_s (assuming a perfectly linear relationship between R_s and period) (3). On the other hand, the term arising from the bias currents, (4), is proportional to the period with the addition of the energy used by the digital devices E_{DIGITAL}, namely, U3 and the counter. Finally (5), results from the substitution of (3) and (4) in (2)

$$EPC = E_{\text{sensor}} + E_{\text{interface}} = T \cdot (P_{\text{sensor}} + P_{\text{interface}}) \quad (2)$$

$$E_{\text{sensor}} = \frac{2 \cdot C \cdot \delta \cdot V_{\text{HIST}} \cdot V_{\text{DD}}}{V_{\text{REF}}} \quad (3)$$

$$E_{\text{interface}} = \frac{2 \cdot V_{\text{DD}} \cdot R_s \cdot C \cdot \delta \cdot V_{\text{HIST}} \cdot \Sigma I}{V_{\text{REF}}} + E_{\text{DIGITAL}} \quad (4)$$

$$\begin{aligned} EPC = & 2 \cdot V_{\text{DD}} \cdot C \cdot \delta \cdot V_{\text{HIST}} \cdot \left(\frac{1 + R_s \cdot \Sigma I}{V_{\text{REF}}} \right) \\ & + E_{\text{DIGITAL}}. \end{aligned} \quad (5)$$

The large input range required to interface chemiresistive gas sensors leads to a difference of EPC of several decades along R_s full range. A simulated example of such behavior is presented in Fig. 2 for three values of total bias currents (ΣI). The relationship between EPC and R_s evolves as R_s increases: for low values of R_s, the oscillation frequency is highest (1), and the fraction of the energy dissipated in the sensor is dominant (3) because the sensor current is very large (constant EPC). When R_s is over a given corner point, the current through the sensor becomes smaller than the sum of the bias currents ΣI, and EPC surges. When R_s · ΣI ≫ 1 the EPC is proportional to the sensor resistance (5), as seen on the right side of Fig. 2. As the energy to toggle an inverter (U3) is in the order of tenths of fJ for a 180 nm process, E_{DIGITAL}

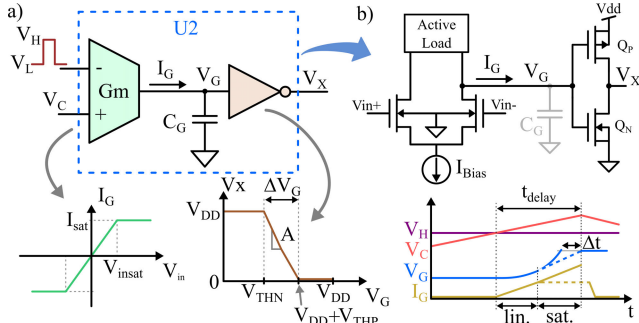


Fig. 3. (a) Block diagram of the comparator with the transfer function of each device. V_{THN} and V_{THP} are the threshold voltages of nMOS and pMOS transistors, respectively. (b) Schematic of a generic comparator and time-domain signals at different nodes.

is mainly due to the counter. Microcontrollers typically used in IoT systems embed counters that are highly programmable and offer automatic time measurements functionalities even while in sleep mode. We thus have preferred this approach for our designs focused on ASICs that are not yet available for system implementation. For this reason, the counter is left out of the scope of this work and consequently its effect on EPC. V_{REF} is also supplied externally, and not accounted for in EPC. Nevertheless, we verified from [26] and by simulations that well-known designs of V_{REF} generators in 180 nm CMOS would not add a significant EPC term, higher than the ones we consider.

From an efficiency point of view, once a technology node is chosen, decreasing V_{DD} does not provide an ample margin for lowering EPC, even less in nanometer nodes. Furthermore, C , V_{HIST} , and δ have the same effect: they trade lower EPC for higher oscillation frequency for a given R_s . Consequently, assuming that the circuit is already designed to reach the maximum allowable frequency set by external requirements, like the microcontroller maximum clock speed, there is no room to lower EPC with these parameters [6].

The only parameter that has no impact on oscillation frequency is the total bias current, which is predominantly the sum of that of U1 and U2. The voltage regulator has a unity gain and U1 drives a MOS transistor, so there's no dc output current flowing from U1. Additionally, gas sensing applications require a low bandwidth since gas concentrations usually fluctuate at frequencies in the hertz-range and the sensors have also their intrinsic response time. Consequently, U1 can be biased with a very small current, as only a small open-loop gain is needed to guarantee stability. Therefore, the bias current of U2 becomes the most detrimental parameter for the EPC. The scaling of this current is bounded by the response time of the comparator and the acceptable nonlinearity added to the resistance-to-period transfer function (1).

B. Bias Current Sizing

The maximum attainable frequency by the ROIC is set by the comparator delay, therefore it is important to size it properly in relation to the oscillation period but without overreaching, as this would require a larger bias current and efficiency would be degraded. In this section, we explain how to size the bias current using the simplified model of Fig. 3.

Comparators have been extensively researched and countless implementations have been proposed [27], [28], [29]. To keep the analysis as general as possible, we consider a basic comparator architecture: a differential transconductor, G_m , drives a high-gain amplifier, like a digital inverter whose output toggles between V_{DD} and ground upon a small change of its input voltage, Fig. 3(a). G_m is modeled as a MOSFET differential pair with an active load where one input is connected to the integration capacitor C and the other toggles between two voltages V_H and V_L : $V_{HIST} = V_H - V_L$ in sync with the output. The transconductance is determined by the transistor's geometry and bias current, which also sets the maximum sink and source output current drive, I_{sat} .

The high-gain amplifier (e.g., a digital inverter), can be modeled by a gain A and a capacitor C_G at its input, that mimics the pole at that node, Fig. 3(a). To toggle the output of the amplifier from one digital value to the other, G_m must charge or discharge C_G , by $\Delta V_G = V_{DD} + V_{THP} - V_{THN}$, Fig. 3(a). The process of charging V_G is depicted in Fig. 3(b). After the differential input of the comparator crosses zero, I_G increases and so does V_G . Here, two different situations may occur depending on I_{sat} and the slew rate of V_C . In one scenario [dashed line in Fig. 3(b)], G_m saturates at I_{sat} before C_G is fully charged, increasing the delay by Δt , in the other situation (solid line), G_m does not saturate, and V_G has a parabolic shape achieving a lower delay. These delays are calculated in (6) and (7) for each case, respectively, using the equations of the devices, Fig. 3(a)

$$\Delta t = \sqrt{\frac{2 \cdot \Delta V_G \cdot C_G \cdot R \cdot C \cdot \delta}{g_m \cdot V_{REF}}} \quad (6)$$

$$\Delta t = \frac{2 \cdot g_m \cdot V_{REF} \cdot C_G \cdot \Delta V_G + I_{sat}^2 \cdot R \cdot \delta \cdot C}{2 \cdot I_{sat} \cdot g_m \cdot V_{REF}} \quad (7)$$

$$\frac{t_0}{T} = \sqrt{\frac{2 \cdot V_{sat} \cdot C_G \cdot V_{REF}}{g_m \cdot R \cdot \delta \cdot C}} \frac{1}{V_{HIST}} \quad (8)$$

$$\frac{t_0}{T} = \frac{I_{sat} \cdot C_G}{I_{sat} \cdot R \cdot C \cdot \delta \cdot V_{HIST}} + \frac{1}{2 \cdot g_m \cdot V_{REF} \cdot V_{HIST}}. \quad (9)$$

With (2), (6), and (7), the delay-to-period ratio takes the form of (8) in linear region and is aggravated when G_m saturates (9). In Fig. 4(a), curves (8) and (9) as well as the EPC are plotted taking the technology parameters from a commercial 180 nm silicon-on-insulator (SOI) process. The dashed parts, Fig. 4(a), indicate saturation of G_m and in turn a faster increase of the delay. In terms of EPC, Fig. 4(c), a bathtub-like shape appears for a 100 nA bias because the period does not decrease as fast as the resistance does, due to the delay taking a constantly increasing fraction of the period, which hinders operation at higher frequencies. Consequently, nonlinearity is aggravated, and SNR reduced as T is less sensitive to R .

Chemiresistive gas sensors are generally nonlinear devices [30] which require the knowledge of its response curve to make precise gas measurements from their estimated resistance. Taking advantage of this, the ROIC nonlinearity can be accounted for in the sensor calibration curve. In this manner, nonlinearity requirements are less stringent and power

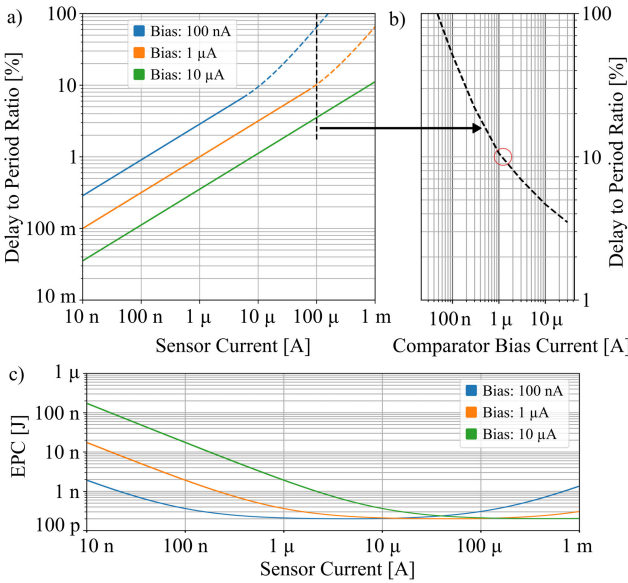


Fig. 4. (a) Comparator delay for three bias currents. Simulation parameters: $V_{\text{REF}} = 1 \text{ V}$, $C = 8 \text{ pF}$, $\delta = 10$, $V_{\text{DD}} = 1.8 \text{ V}$, and $V_{\text{HIST}} = 0.6 \text{ V}$. Technology: X-FAB 180 nm. (b) Fractional delay versus comparator bias for: $I_{\text{sensor}} = 100 \mu\text{A}$ ($V_{\text{REF}} = 1 \text{ V}$ and $R_s = 10 \text{ k}\Omega$) with G_m : $W = 1 \mu\text{m}$, $L = 500 \text{ nm}$, Inverter: $W = 500 \text{ nm}$, $L = 500 \text{ nm}$. $C_{\text{inv}} = 29.5 \text{ fF}$, g_m from technology's g_m/d curves (27.3 μS at 1.5 μA). (c) EPC with the same parameters as in (a).

consumption can be kept low. We chose to limit nonlinearity to 10% to safeguard the $\Delta T/\Delta R$ gain factor and the SNR.

To keep quantization noise close to SNR at maximum frequency, the ROICs presented in the coming sections have been designed to oscillate at frequencies going up to 1 MHz, limited by the microcontroller's clock frequency. In Fig. 4(b), I_{sat} , which is equal to the comparator bias, is taken as the independent variable and the period-delay ratio plotted again, for $I_{\text{Sensor}} = 100 \mu\text{A}$, which is the maximum sensor current by design. From this chart, we determine that a bias current close to 1.5 μA is required to achieve an adequate delay, below 10% of the oscillation period. This value provides a good initial estimation. In practice, full-circuit simulations have shown that a value closer to 3 μA is more adequate. With this value of I_{bias} , the EPC has the aforementioned characteristic, spanning slightly more than two decades from its lowest value, Fig. 4(c).

Due to the need to integrate a large number of sensors in the same package, miniaturization is paramount. However, this results in an increase of the resistance of each device, reducing the sensor current and operating the ROIC where it is least efficient. To tackle this problem, in Section III, we propose two adaptive biasing techniques that help diminish the EPC when R_s is highest, without affecting the transfer characteristics.

III. ADAPTIVE BIASING TECHNIQUES

- 1) The first method is based on the observation that the comparator needs to be biased only when a switching event is imminent. To achieve this, we designed a zero-crossing bias (ZXB) current generator, Fig. 5, where the current sourced by Q9 to bias the comparator is maximum when the comparator inputs V_+ and V_- are equal. The currents and voltages are plotted in Fig. 6. To the

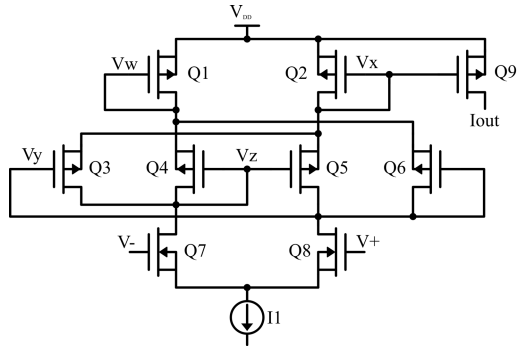


Fig. 5. ZXB current generator schematic. Sizes (W/L) $Q1 = Q2 = 500 \text{ nm}/500 \text{ nm}$, $Q3 = Q4 = Q5 = Q6 = 700 \text{ nm}/700 \text{ nm}$, $Q7 = Q8 = 220 \text{ nm}/10 \mu\text{m}$, and $Q9 = 3.75 \mu\text{m}/220 \text{ nm}$.

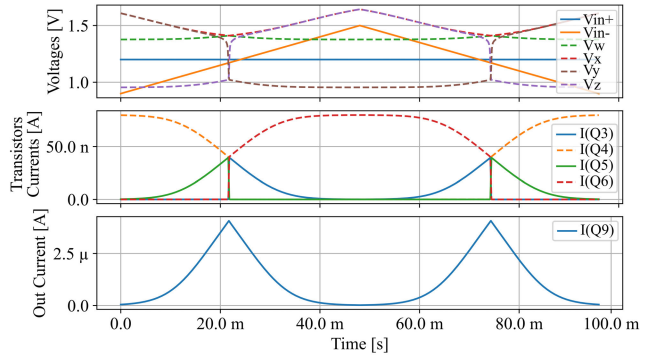


Fig. 6. Time-domain simulated current and voltages in the ZXB of Fig. 5 for one period of 10 Hz triangle waveform.

best of our knowledge, this is the first time such circuit is presented in the literature.

The differential stage is biased with an 80 nA current source continuously. When the voltages at the gates are dissimilar, the current flows either through Q4 or Q6, both connected to Q1, so there is no current flowing through Q2. When the gates of Q7 and Q8 are at the same voltage, then the current flows equally through Q3 and Q5 or Q4 and Q6. This results in a spike-shaped current in Q2 with a peak amplitude of 40 nA. To produce a larger current, Q9 is enlarged with respect to Q2, resulting in a peak current of over 3 μA , Fig. 6. The quiescent current is 80 nA.

The overall benefit of using the ZXB is shown in Fig. 7, where the ratio of peak to average total consumed current is plotted. For low slew-rates this circuit produces a peak bias current more than three times the average current consumption.

Compared to other adaptive biasing techniques, this circuit offers excellent transient response, and it can operate with input slew rates above 1 $\text{V}/\mu\text{s}$. On the contrary, in [31] a comparator with an adaptive bias current generator was proposed and tested in a 350 nm technology, reaching a maximum frequency of 130 kHz with a quiescent current of 33 nA. In the cited paper, the adaptive bias is generated using current subtractors that copy and amplify the currents flowing through diode-connected transistors that are part of the hysteresis mechanism of the comparator. The main drawback is that the current in these transistors increases with a delay due

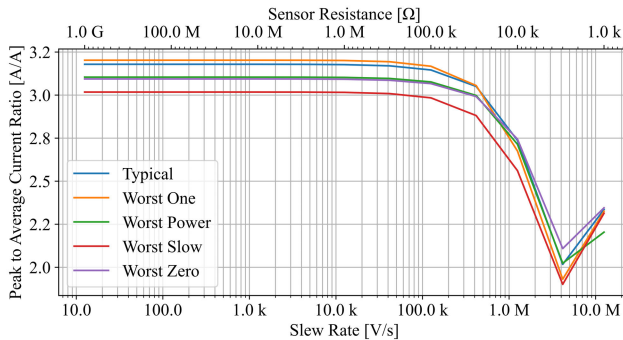


Fig. 7. Ratio of improvement of using the ZXB compared to a fixed bias current, simulated for all corners and the corresponding sensor resistance when $V_{\text{REF}} = 1 \text{ V}$.

to the hysteresis and consequently the adaptive bias generation is also delayed.

2) The second adaptive biasing technique we propose takes a different approach, noting that the delay requirement of the comparator changes with the sensor's resistance as it sets the slew rate of the V_c , Fig. 2. For low values of R_s , the oscillation frequency is highest and so the bandwidth requirement of the comparator, the opposite happens for highest resistances. With this in mind, we propose to bias the comparators with the sum of two sources: a 100 nA fixed source and a reduced copy of the sensor current. Consequently, a larger current will be generated when a larger bandwidth in the comparator is needed. To obtain a maximum bias current close to $3 \mu\text{A}$, a reduction factor of 30 was selected since the maximum sensor current is designed to be $100 \mu\text{A}$ ($V_{\text{REF}} = 100 \text{ mV}$, $R_s = 1 \text{ k}\Omega$). The fixed current is a scaled copy of the externally supplied reference current, which is already used in the ROIC to bias all the active devices by a set of current mirrors.

IV. IMPLEMENTATIONS AND MEASUREMENTS

Two readout circuits for resistive gas sensors, named ULP1 and ULP2, were implemented in a 180 nm SOI process, XT018 from X-FAB (X-FAB Semiconductor Foundries GmbH, Erfurt, Germany), Fig. 8(b). The areas of these two ROICs are 0.183 and 0.119 mm^2 , respectively. They were designed to handle sensor currents, V_{REF}/R_s , from 1 nA up to $100 \mu\text{A}$ with V_{REF} ranging from 50 mV to 1 V. The principle of operation is that of Fig. 1 but structurally ULP1 and ULP2 have some differences. Instead of using a Schmitt trigger comparator, two regular comparators with nMOS and pMOS input differential pairs, respectively, were used to allow for better control of the threshold voltages. Additionally, an SR latch was added at the output to avoid false toggles generated by noise that could induce jitter. To study the robustness in the copy of the sensor current used to charge and discharge C , ULP1 uses cascade-regulated current mirrors while ULP2 uses standard cascodes, the former being more linear for currents in the nA-range. Both circuits share the same design parameters: $C = 8 \text{ pF}$, $\delta = 10$, $V_H = 1.2 \text{ V}$, $V_L = 0.6 \text{ V}$. The reference voltages for the comparators V_H and V_L were generated with on-chip $M\Omega$ resistors, consuming 55 nA, V_{REF} is supplied

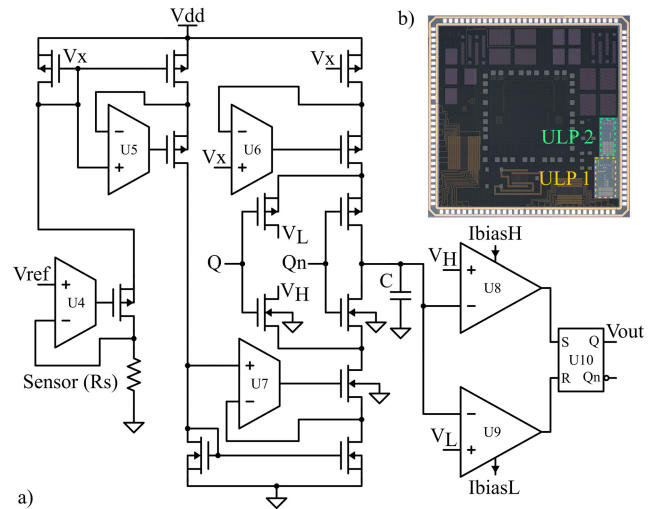


Fig. 8. (a) Schematic of readout ULP1, the comparators are biased with ZXBs. (b) Photograph of the fabricated integrated circuit containing both ASICs.

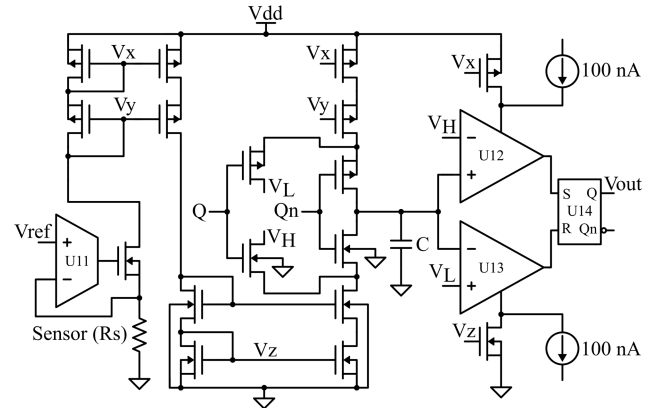


Fig. 9. Schematic of readout ULP2, the comparators are biased with a fixed 100 nA plus a reduced copy of the current through the sensor.

externally. The capacitors are all metal-insulator-metal (MIM) type. For the circuit characterization, discrete resistors ranging from $1 \text{ k}\Omega$ up to $1 \text{ G}\Omega$ were used.

ULP1, Fig. 8(a), uses active current mirrors and the ZXB technique in both complementary comparators. The transconductors used in the regulated current mirrors (U5, U6, and U7) are biased with 10 nA each, having little impact on the overall power consumption. ULP2, Fig. 9, relies on biasing the comparators with a reduced copy of the sensor current plus a 100 nA dc source (not present in ULP1), as explained earlier. In this way, the comparators are biased with at most $3.3 + 0.1 \mu\text{A}$. When the current in the sensor is minimum, 1 nA, essentially only the fixed 100 nA remains.

The measured transfer functions as well as the simulated corners and the ideal response are plotted in Fig. 10 for both circuits, ten chip samples each, biased with 50 mV and 1 V. The plots present the average values and standard deviation, the latter not being noticeable. The maximum nonlinearity in the full characterization range is -32% for ULP1 and 41% for ULP2. If the nonlinearity is restricted to $\pm 10\%$ (shaded area in Fig. 10), the input range of ULP1 extends from $2.4 \text{ k}\Omega$

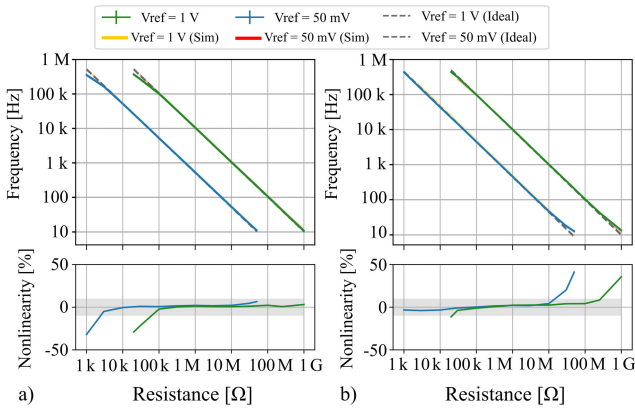


Fig. 10. Measured, simulated, and ideal transfer functions for (a) ULP1 and (b) ULP2, the measured transferred functions are compared to the ideal response in the nonlinearity plots. Ten chips were measured and averaged. The error bars, although small, are also plotted. The shaded area indicates nonlinearity within 10%.

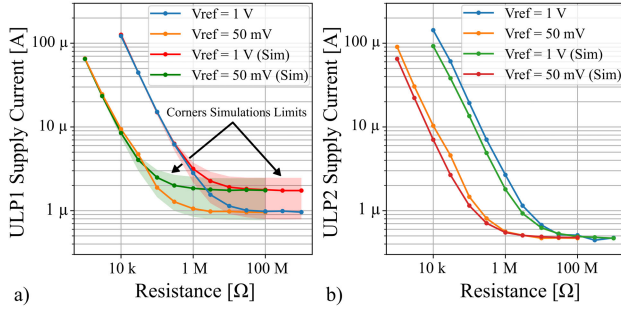


Fig. 11. Measured and simulated supply current for (a) ULP1 and (b) ULP2. Corners bounds are represented by the shaded area.

to $1\text{ G}\Omega$ and from $1\text{ k}\Omega$ to $270\text{ M}\Omega$ for ULP2. For largest resistances, the benefit of using active current mirrors results in a more precise copy of the sensor current and in turn better linearity, at the cost of larger die area due to the additional $9600\text{ }\mu\text{m}^2$ needed for MIM capacitors (22.7 pF) to guarantee stability. At such low currents, the V_{DS} in the diode-connected devices is only some tenths of mV so, a significantly larger V_{DS} in the passive copying transistor results in large differences in the current through the drain. The active current mirrors help diminish the difference between both V_{DS} to just the offset voltage of the transconductor. The nonlinearity at high currents is mostly explained by the tradeoff presented in Section III regarding comparators bias and delay. Notably, ULP2 performs better, the reason for this is that at $1\text{ k}\Omega$ the ZXB is operating with an input slew rate of $0.42\text{ V}/\mu\text{s}$, where its efficacy declines, Fig. 7.

The total average supply current for ULP1 and ULP2 are plotted in Fig. 11, due to the dominance of the sensor current for lowest sensor's resistances, the curves are almost identical in this region. A larger variation with process corners is predicted by simulations in ULP1 when the sensor current vanishes after the corner point, because small size transistors are used for the ZXB to obtain the best frequency response, making it more vulnerable to process variations.

The supply current difference between ULP1 and ULP2 above $100\text{ M}\Omega$ is explained by the biasing current in the

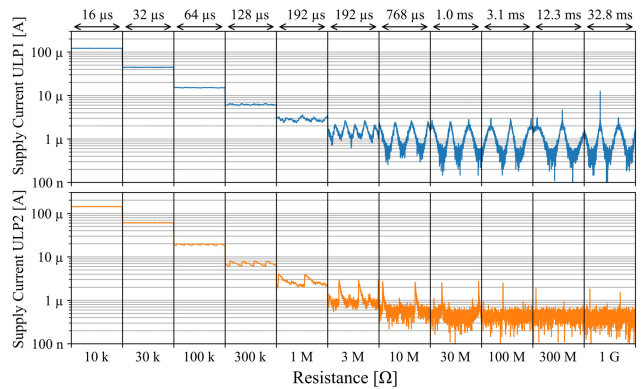


Fig. 12. Time fragments of the current drawn from the main supply for a range of resistances and $V_{\text{REF}} = 1\text{ V}$.

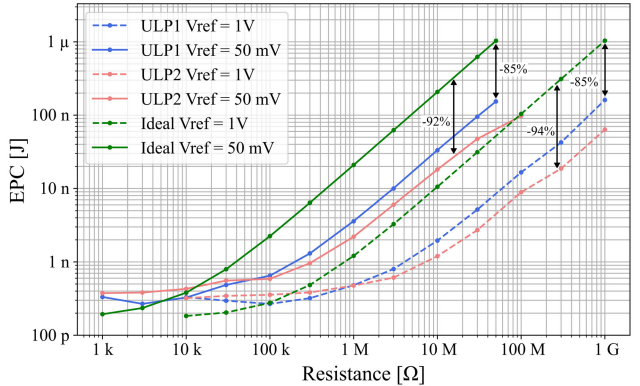


Fig. 13. Measured EPC for ULP1 and ULP2 compared to an ideal readout interface whose comparators are biased with $3\text{ }\mu\text{A}$ dc each.

comparators: in ULP2 both comparators are biased with a 100 nA fixed source each (the current copied from the sensor is negligible), while in ULP1 the ZXB still consumes on average $1\text{ }\mu\text{A}$. The rest of the devices: U1, U2, U3, and U4 consume 10 nA , not affecting the analysis significantly. Time records of a few oscillation cycles of the current drawn from V_{DD} are plotted in Fig. 12, for $V_{\text{REF}} = 1\text{ V}$. The operation of the ZXB is clearly visible for R_s larger than $3\text{ M}\Omega$. For ULP2 short spikes are seen which can be attributed to the charge/discharge cycles of the embedded decoupling capacitors and switching of the SR latch.

The EPC is calculated from the current and frequency measurements, ($V_{\text{REF}} = 50\text{ mV}$ and 1 V) for both designs, Fig. 13. As the current generated by either of the two bias generation mechanisms is close to $3\text{ }\mu\text{A}$ at its maximum point, we compare the EPC of ULP1 and ULP2 to an ideal design whose comparators are biased with a constant $3\text{ }\mu\text{A}$ dc source. The results show that when the sensor resistance is low the EPC of the three circuits are similar but great gains are observed for the largest sensor resistance, where the EPC drops almost one decade for ULP1 and more than one decade for ULP2, i.e., 85% and 94% lower with respect to dc biasing, respectively. A shift to the right of the corner point in (5) is also seen. Due to the different onset of action of each adaptive biasing mechanism, the shape of EPC is slightly different, having a similar but not equal slope in the rising part. For

TABLE I
STATE OF THE ART COMPARISON

Type	This work (ULP1)	This work (ULP2)	JSEN 2022 [6]	JSEN 2019 [11]	TIE 2020 [20] a)	TIE 2020 [20] b)	VLSI Circuit 2015 [24]	JSSC 2020 [32]	TCASII 2020 [33]
Technology (m)	180 n	180 n	180 n	130 n	180 n	180 n	180 n	180 n	65 n
Input range (Ω)	2.4 k-1 G	1 k-270 M	1 k-33 M	100-1 M	250 k-2 M	8 k-2M	10 k-10 M	0.02 k-20 k	1 k-100 k
Power (W)	$1.8 \mu^1$	$900 n^1$	$364 \mu^1$	$680 \mu^1$	$2.95 \mu^2$	$2.51 m$	1.7μ	171μ	$44.5 n\text{-}69.5 n^1$
EPC (J)	$268 p\text{-}161 n^3$	$321 p\text{-}65 n^3$	$1.21 n\text{-}188 n^3$	$150 p\text{-}675 n^3$	$89.5 p^2$	$24.9 n^2$	$1.42 n$ (worst)	$34.2 n$	$4.7 n$
FOM [12] (J/c.s.)	232 f-78 p	219 f-177 p	2.09 p-129 p	32.6 f-148 p	0.53 p	1.43 p	-	1.48 p	2.54 p-3.03 p
SNR (dB)	55-70	54-68	56-65	62-75	46.3	86.6	53.6 ⁴	89	65.6
Nonlinearity	10 %	10 %	-	0.4 %	-	-	0.21 %	0.005 %	0.4 %

¹ Does not include the power dissipated in the sensor.

² Sensor heater current of $118.8 \mu A$ not included.

³ Does not include the energy consumed by the counter.

⁴ Not reported directly, calculated from the worst-case measurement error of 0.21 %.

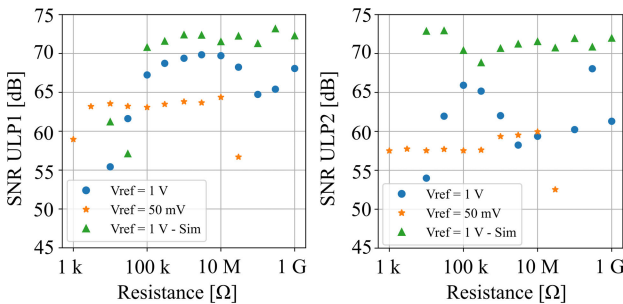


Fig. 14. Measured and simulated SNR for ULP1 and ULP2 for discrete resistors: 1 k Ω , 3 k Ω , 10 k Ω , 30 k Ω , 100 k Ω , 300 k Ω , 1 M Ω , 3 M Ω , 10 M Ω , 30 M Ω , 100 M Ω , 300 M Ω , and 1 G Ω .

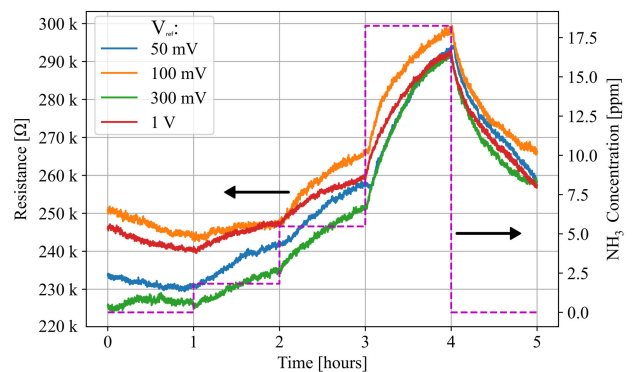


Fig. 15. Ammonia detection test with a ULP1 and a PPy sensor. Four bias voltage and three ammonia concentration were employed.

$V_{REF} = 50 \text{ mV}$, and $R_s = 100 \text{ M}\Omega$, there is a decrease in the slope of ULP2 explained by the nonlinearity in the transfer function. The oscillation frequency is larger than the ideal, so the integration time of the consumed current is smaller. For the highest frequency, ULP2 offers no benefit in comparison to dc biasing, on the other hand the ZXB in ULP1 is still operating and leads to a slightly lower EPC than the former.

To calculate the SNR, 4096 consecutive period measurements were done for each point of operation and the SNR calculated from the jitter, Fig. 14. Due to the measurement setup, the noise of the test resistor could not be removed. Sensors made with conductive polymers and graphene tend to be moderately noisy devices, for example, in our measurements of Fig. 14, the SNR of the PPy sensor is 56 dB, for PANI sensors we have measured an SNR of 30 dB. In [11], a minimum SNR of 46 dB was reported for MOx sensors also. These values are below ULP1 and ULP2 intrinsic noise, confirming the suitability of these circuits to interface gas sensors. The calculated dynamic ranges are listed in Table I, exceeding 128 dB [11] in all cases.

ULP1 was used in combination with a PPy sensor to estimate ammonia at three different concentrations by calculating the sensor resistance from the measured output frequency, Fig. 15. Four different bias voltages were employed demanding different EPCs for the same sensor, according to Fig. 13. For this sensor, the response time, noise, and sensitivity are not affected considerably by the bias voltage, so the

largest V_{REF} produces the lowest EPC. The counter used for these measurements as well as the SNR is from an STM32 STM32L4R5ZI microcontroller.

Table II compares the performance of ULP1 and ULP2 to relevant ROICs developed recently for resistive sensors. Our designs present the largest input resistance range, needed to accommodate diverse chemiresistive sensors and improve sensing performance by expanding the scope of usable sensors.

The most similar architectures to our ROICs are that of [6] and [11] which resemble relaxation-oscillator but without adaptive biasing, this is evident noting that for 1 k Ω the EPC is similar with respect to ULP2, but at 33 M Ω , [6] has twice the EPC and at 1 M Ω , [11] has an EPC over 100 \times larger. The SNR is similar to that of ULP1 and ULP2, peaking at 75 dB. Both [6] and [11] use an external counter. As expected from its wide input range and lack of feedback, open-loop oscillators present the most nonlinearity, being ULP1 and ULP2 the least linear followed by [12] with 0.5% and [11] with 0.4%.

TABLE II
DYNAMIC RANGE

Sensor Bias Voltage	ULP1	ULP2
50 mV	142 dB	136 dB
1 V	139 dB	135 dB

In [24], a disruptive logarithmic fast-response circuit is presented, only the worst EPC of 1.42 nJ is reported. This circuit is particularly interesting because with the usage of nonlinear decision circuits the time it takes to find the appropriate bias point has been shortened and as a result a low EPC is achieved while using an IDAC + ADC architecture. In general, the measurement process of ADC-based ROICs is less time dependent than oscillator-based ROIC, hence the EPC more homogenous. As with other closed-loop approaches the sensor bias point is dictated by the feedback loop and the SNR is limited by the number of bits.

Another closed-loop ROIC was introduced in [32]. It has an excellent SNR of 89 dB which was achieved by using a second loop in a sturdy multistage noise shaping configuration. The linearity, at 14 bits, is also remarkable. On the other hand, the digital processing needed to achieve such SNR makes the EPC one of the highest in the table (at 20 kΩ) and the input range, like in [24], is limited to three decades.

The discharge time or triggered ROIC of [33] provides decent performance with a very simple design but falling short the requirements of gas sensing that our designs target. Even though the EPC and the range are not outstanding, its footprint is, at only 2500 μm^2 .

Finally, two ROICs have been combined in [20] to operate the system in two modes: 1) monitoring (with a relaxation-oscillator) or 2) high precision (with an ADC and an IDAC). In monitoring mode, it presents the lowest EPC of all but is restricted in SNR and input range, limiting the scope of sensors. Even though the performance in monitoring mode is not sufficient alone, this work reinforces the suitability of relaxation-oscillator for low power applications. The high precision read-out improves input range and SNR significantly at the expense of a larger EPC.

All the discussed relaxation oscillator ROICs: ULP1, ULP2, [6], [11], [12] use an external counter therefore the EPC does not fully account the whole acquisition-digitization process and comparison with the other types of ROICs is limited in this aspect.

In the case the counter shall be integrated, simulations in 180 nm show that 12-bit counters with a current consumption of 194 nA/MHz are possible using D type flip-flops. When compared to the EPC curves of the ROICs it mainly impacts the high frequency power consumption where the ROICs EPC is at its lowest. The difficulty of this approach is to have more than one clock source available on chip. On the other hand, this is standard for microcontrollers where multiple clock sources, phase-locked loop (PLL) configurations, and prescalers are available.

V. CONCLUSION

This article addresses the power and efficiency challenges that gas sensors present for ultralow-power systems. The state-of-the-art readout circuits have been reviewed and we confirm that adaptive biasing is critical to make open-loop-relaxation-oscillator-based ROICs more efficient. The two techniques we describe improve efficiency for large resistance sensors in a similar scale, reducing EPC down to a tenth versus standard dc biasing. No other published work presented simultaneously

ultralow power, over five decades input range, and an SNR above 55 dB. The sensor-current-proportional biasing (ULP2) yielded the largest improvement on EPC and was least affected by process variations. ZXB offers a significant improvement throughout the whole frequency range, at the expense of larger process, voltage and temperature (PVT) variations. In all, these techniques are not mutually exclusive and a combination of both could be feasible. The effect of active and passive current mirrors was also researched, and we can conclude that active current mirrors can diminish nonlinearity for nA sensor currents with a small penalty in the EPC of 9 nJ (in a total of 161 nJ for 1 GΩ). Finally, ULP1 was successfully tested with a PPy sensor to measure different concentrations of ammonia at different bias voltages, confirming the performance from a practical standpoint.

REFERENCES

- [1] J. Haldane, "The detection and estimation of carbonic oxide in air," *J. Physiol.*, vol. 20, no. 6, pp. 521–522, Dec. 1896.
- [2] G. Neri, "First fifty years of chemoresistive gas sensors," *Chemosensors*, vol. 3, no. 1, pp. 1–20, Jan. 2015.
- [3] Y. C. Wong, B. C. Ang, A. S. Hasseeb, A. A. Baharuddin, and Y. H. Wong, "Review-conducting polymers as chemiresistive gas sensing materials: A review," *J. Electrochem. Soc.*, vol. 167, no. 3, 2019, Art. no. 037503.
- [4] R. Ghosh, M. Aslam, and H. Kalita, "Graphene derivatives for chemiresistive gas sensors: A review," *Mater. Today Commun.*, vol. 30, Mar. 2022, Art. no. 103182.
- [5] Dräger Safety AG & Co. KGaA. (2008). *Introduction to Gas Detection Systems*. [Online]. Available: <https://www draeger.com/library/content/introduction-gds-fl-9046421-en.pdf>
- [6] R. Puyol, S. Pétré, Y. Danlée, T. Walewyns, L. A. Francis, and D. Flandre, "An ultra-low-power read-out circuit for interfacing novel gas sensors matrices," *IEEE Sensors J.*, vol. 22, no. 10, pp. 9521–9533, May 2022.
- [7] D. A. Hall, R. S. Gaster, K. A. A. Makinwa, S. X. Wang, and B. Murmann, "A 256 pixel magnetoresistive biosensor microarray in 0.18 μm CMOS," *IEEE J. Solid-State Circuits*, vol. 48, no. 5, pp. 1290–1301, May 2013.
- [8] P. Le Maout et al., "Polyaniline nanocomposites based sensor array for breath ammonia analysis. Portable e-nose approach to non-invasive diagnosis of chronic kidney disease," *Sens. Actuators B, Chem.*, vol. 274, pp. 616–626, Nov. 2018.
- [9] L. Ge et al., "A fully inkjet-printed disposable gas sensor matrix with molecularly imprinted gas-selective materials," *npj Flexible Electron.*, vol. 6, no. 1, p. 1, Jun. 2022.
- [10] N. P. Simonenko et al., "Printing technologies as an emerging approach in gas sensors: Survey of literature," *Sensors*, vol. 22, no. 9, p. 3473, May 2022.
- [11] F. Ciciotti et al., "A 450- μA 128-dB dynamic range A/D CMOS interface for MOX gas sensors," *IEEE Sensors J.*, vol. 19, no. 24, pp. 12069–12078, Dec. 2019.
- [12] A. V. Radogna, S. Capone, L. Francioso, P. A. Siciliano, and S. D'Amico, "A 296 nJ energy-per-measurement relaxation oscillator-based analog front-end for chemiresistive sensors," *IEEE Trans. Circuits Syst. I, Reg. Papers*, vol. 68, no. 3, pp. 1123–1133, Mar. 2021.
- [13] E. Sacco, J. Vergauwen, and G. Gielen, "A 96.9-dB-resolution 109- μW second-order robust closed-loop VCO-based sensor interface for multiplexed single-ended resistance readout in 180-nm CMOS," *IEEE J. Solid-State Circuits*, vol. 57, no. 9, pp. 2764–2777, Sep. 2022.
- [14] E. Sacco, J. Vergauwen, and G. Gielen, "From open-loop to closed-loop single-VCO-based sensor-to-digital converter architectures: Theoretical analysis and comparison," in *Proc. IEEE 8th Int. Workshop Adv. Sensors Inter. (IWASI)*, Jun. 2019, pp. 29–34.
- [15] H. Xin, M. Andraud, P. Baltus, E. Cantatore, and P. Harpe, "A 0.34–571 nW all-dynamic versatile sensor interface for temperature, capacitance, and resistance sensing," in *Proc. IEEE 45th Eur. Solid State Circuits Conf. (ESSCIRC)*, Sep. 2019, pp. 161–164.

- [16] B. Li, J.-P. Na, W. Wang, J. Liu, Q. Yang, and P.-I. Mak, "A 13-bit 8-kS/s Δ - Σ readout IC using ZCB integrators with an embedded resistive sensor achieving 1.05-pJ/conversion step and a 65-dB PSRR," *IEEE Trans. Very Large Scale Integr. (VLSI) Syst.*, vol. 27, no. 4, pp. 843–853, Apr. 2019.
- [17] S. Oh et al., "A 2.5 nJ duty-cycled bridge-to-digital converter integrated in a 13 mm³ pressure-sensing system," in *IEEE Int. Solid-State Circuits Conf. (ISSCC) Dig. Tech. Papers*, Feb. 2018, pp. 328–330.
- [18] S. Choi et al., "A wide dynamic range multi-sensor ROIC for portable environmental monitoring systems with two-step self-optimization schemes," *IEEE Trans. Circuits Syst. I, Reg. Papers*, vol. 68, no. 6, pp. 2432–2443, Jun. 2021.
- [19] K.-C. Woo and B.-D. Yang, "0.3-V RC-to-digital converter using a negative charge-pump switch," *IEEE Trans. Circuits Syst. II, Exp. Briefs*, vol. 67, no. 2, pp. 245–249, Feb. 2020.
- [20] K. Park et al., "An energy-efficient multimode multichannel gas-sensor system with learning-based optimization and self-calibration schemes," *IEEE Trans. Ind. Electron.*, vol. 67, no. 3, pp. 2402–2410, Mar. 2020.
- [21] É. Morin, M. Maman, R. Guizzetti, and A. Duda, "Comparison of the device lifetime in wireless networks for the Internet of Things," *IEEE Access*, vol. 5, pp. 7097–7114, 2017.
- [22] B. Saruhan, R. L. Fomekong, and S. Nahiriak, "Review: Influences of semiconductor metal oxide properties on gas sensing characteristics," *Frontiers Sensors*, vol. 2, pp. 6–11, Apr. 2021.
- [23] F. Ciciotti, C. Buffa, R. Gaggli, and A. Baschirotto, "A programmable dynamic range and digital output rate oscillator-based readout interface for MEMS resistive and capacitive sensors," in *Proc. Int. Conf. IC Design Technol. (ICICDT)*, Jun. 2018, p. 44.
- [24] M. Choi, J. Gu, D. Blaauw, and D. Sylvester, "Wide input range 1.7 μ W 1.2 kS/s resistive sensor interface circuit with 1 cycle/sample logarithmic sub-ranging," in *Proc. Symp. VLSI Circuits (VLSI Circuits)*, Jun. 2015, p. C331.
- [25] R. H. Walden, "Analog-to-digital converter survey and analysis," *IEEE J. Sel. Areas Commun.*, vol. 17, no. 4, pp. 539–550, Apr. 1999.
- [26] H. Zhuang, X. Liu, and H. Wang, "Voltage reference with Linear-Temperature-Dependent power consumption," *IEEE Trans. Very Large Scale Integr. (VLSI) Syst.*, vol. 28, no. 4, pp. 1043–1049, Apr. 2020.
- [27] R. J. Baker, "Nonlinear analog circuits," in *Circuit Design, Layout, and Simulation*, 4th ed. Hoboken, NY, USA: Wiley, 2019, pp. 933–954.
- [28] T. Saito and S. Komatsu, "A low—Voltage hysteresis comparator for low power applications," in *Proc. 24th IEEE Int. Conf. Electron., Circuits Syst. (ICECS)*, Dec. 2017, pp. 427–430.
- [29] X. Qian and T. H. Teo, "A low-power comparator with programmable hysteresis level for blood pressure peak detection," in *Proc. IEEE Region Conf. (TENCON)*, Jan. 2009, pp. 1–4.
- [30] Z.-F. Li, F. D. Blum, M. F. Bertino, and C.-S. Kim, "Understanding the response of nanostructured polyaniline gas sensors," *Sens. Actuators B, Chem.*, vol. 183, pp. 419–427, Jul. 2013.
- [31] K. Isono, T. Hirose, K. Tsubaki, N. Kuroki, and M. Numa, "A 18.9-nA standby current comparator with adaptive bias current generator," in *Proc. IEEE Asian Solid-State Circuits Conf.*, Nov. 2011, pp. 237–240.
- [32] E. Sacco, J. Vergauwen, and G. Gielen, "A 16.1-bit resolution 0.064-mm² compact highly digital closed-loop single-VCO-based 1-1 sturdy-MASH resistance-to-digital converter with high robustness in 180-nm CMOS," *IEEE J. Solid-State Circuits*, vol. 55, no. 9, pp. 2456–2467, Sep. 2020.
- [33] K.-C. Woo and B.-D. Yang, "0.3-V RC-to-digital converter using a negative charge-pump switch," *IEEE Trans. Circuits Syst. II, Exp. Briefs*, vol. 67, no. 2, pp. 245–249, Feb. 2020.



Rafael Puyol (Member, IEEE) received the B.S. and M.S. degrees in electronic engineering from Universidad Católica del Uruguay (UCU), Montevideo, Uruguay, in 2013 and 2018, respectively, where he is currently pursuing the Ph.D. degree in electronic engineering with the Electrical Engineering Department, Université catholique de Louvain (UCLouvain), Louvain-la-Neuve, Belgium.

From 2014 to 2019, he was a Research and Teaching Assistant with the Electric Engineering Department, UCU, and also an Embedded Systems Engineer with BQN, Montevideo. His research interests include the development of ultralow-power integrated circuit for sensors and instrumentation applications.



Thomas Walewyns received the M.Sc. degree in electromechanical engineering from UCLouvain, Louvain-la-Neuve, Belgium, in 2010, the Executive Master in Management degree from the Louvain School of Management, Louvain-la-Neuve, in 2015, and the Ph.D. degree in engineering sciences from UCLouvain, in 2016.

Since 2019, he has been a Co-Founder and the CEO of VOCsens, Louvain-la-Neuve, developing smart gas and environmental microsensor solutions. He has authored or coauthored more than 20 scientific articles and conference papers, and holds three patents. His scientific interests are related to co-integrated CMOS nano-/micro-electromechanical devices (NEMS/MEMS), ultralow-power sensors, autonomous systems, microelectronics, microfabrication, and nanotechnology, with a strong focus on innovation and research valorization.

Dr. Walewyns was the Chair of the UCL IEEE Student Branch Chapter (CASS and EDS) from July 2011 to January 2014. He received the AI-Louvain Innovation Award for his master thesis in 2010.



Laurent A. Francis (Member, IEEE) received the M.Eng. and Ph.D. degrees from the Université catholique de Louvain (UCLouvain), Louvain-la-Neuve, Belgium, in 2001 and 2006, respectively.

He was a Researcher with IMEC, Leuven, Belgium, in the field of acoustic and optical biosensors and piezoelectric RF-MEMS. In 2011, he joined the Université de Sherbrooke, Sherbrooke, QC, Canada, as a Visiting Professor. He is a Professor and a member of the Department, Université catholique de Louvain. He has authored or coauthored more than 150 research articles in international journals. He is a Coeditor of two books and holds five patents. His main focus is on co-integrated, ultralow power CMOS MEMS sensors for biomedical and environmental applications in the frame of the Internet-of-Things and for harsh environments.

Dr. Francis is a Board Member of the Belgian National Committee Biomedical Engineering. He serves as a Treasurer for the IEEE CPMT Benelux Chapter.



Denis Flandre (Senior Member, IEEE) received the M.S. degree in electrical engineering, and the Ph.D. and Habilitation degrees from UCLouvain, Louvain-la-Neuve, Belgium, in 1986, 1990, and 1999, respectively.

His doctoral research was on the modeling of silicon-on-insulator (SOI) MOS devices for characterization and circuit simulation, and his postdoctoral thesis on a systematic and automated synthesis methodology for MOS analog circuits. Since 2001, he has been a full-time Professor with UCL. He has organized or lectured many short courses on SOI technology, devices and circuits in universities, and industrial companies and conferences. He has authored or coauthored more than 1000 technical papers or conference contributions. He is a Co-Inventor of 12 patents. Prof. Flandre is a Co-Founder of CISOID, Mont-Saint-Guibert, Belgium, a UCL spin-off company focusing on SOI and high-reliability integrated circuit design and products. He is Scientific Advisor of other start-ups: INCIZE, Louvain-la-Neuve (Semiconductor characterization and modeling for design of digital, analog/RF and harsh environment applications), e-peas, Louvain-la-Neuve (Energy harvesting and processing solutions for longer battery life, increased robustness in all IoT applications), and VOCsens, Louvain-la-Neuve (smart gas sensing solutions from edge to cloud). He involved in the research and development of SOI MOS devices, digital and analog circuits, as well as sensors, MEMS, and photovoltaic cells, for special applications, more specifically ultralow-voltage low-power, microwave, biomedical, radiation-hardened and high-temperature electronics and microsystems.

Dr. Flandre has received several scientific prizes and best paper awards. He has participated or coordinated numerous research projects funded by regional and European institutions. He has been a member of several EU Networks of Excellence on High-Temperature Electronics, SOI Technology, Nanoelectronics, and Micro-/nano-Technology.